



School of Mathematics and Physics

Title:

**Separating Foregrounds from the Cosmic
Microwave Background**

**Course: BSc (Honours) Degree in Physics Astrophysics &
Cosmology**

Student No: UP844242

Year: 2021

Word count: 2910

School of Mathematics and Physics

DISCLAIMER

The enclosed project is entirely the work of the undergraduate student and any opinions expressed are not necessarily those of any member of the staff of the School of Mathematics and Physics, University of Portsmouth. The text does not show any corrections of fact or calculations, and significant errors and omissions are possible. Any external reader or user of this report does so entirely at their own risk and responsibility, and neither the School of Mathematics and Physics nor the University of Portsmouth can be held responsible for anything contained within this student project report.

Abstract

Through an evolution of methods, this paper aimed to produce a CMB map cleaned of foregrounds of a quality similar to that of Planck's NILC process (Adam, Ade, Aghanim, Arnaud, et al., 2016) for use in deeper CMB analysis. Starting with a full map ILC, a masked version was able to offer comparable variation from a theoretical power spectrum (Lewis et al., 2000), with a percentage error of 15.6% at $\ell = 1500$. An iterative method was developed, however this introduced discontinuity errors, making the system only viable to $\ell \approx 900$. Those errors were not improved with a smoothing function. The final method, performed in needlet space was unable to produce any viable spectrum, due to difficulties recovering a full signal from needlet coefficients.

Contents

1	Introduction	3
2	Theory	4
2.1	Internal Linear Combination	4
2.2	Iterative ILC	5
2.3	Needlet ILC	6
3	Methodology	7
3.1	Synthetic Maps and Bias Estimation	8
3.2	Basic ILC Method	8
3.3	Iterative Method	9
3.4	Needlet Method	9
4	Results	10
4.1	ILC Maps	10
4.2	IILC Maps	11
4.3	NILC Map	12
5	Conclusion	13
6	Appendix	15
6.1	Errors & Synthetic Analysis of the Methods	15
6.2	NILC failings	16
6.3	Excess Tables and Diagrams	18
6.4	Additional Maps	23
6.5	Data	28

List of Figures

1	Galactic foreground emissions as a function of frequency	3
2	Uncleaned Foreground Power Spectra	4
3	WMAP Iterative Regions	6
4	Example Needlet	6
5	Needlet filters	7
6	Synthetic Input Maps	8
7	Filtered 30GHz Input Map	10
8	Basic ILC Power Spectrum	11
9	IILC Smoothed & Unsmoothed 3-year Power Spectra	12
10	NILC Output Power Spectrum	13
11	Needlet Recovery Power Spectrum	17
12	$j = 9$ Observation	17
13	ILC Algorithm Error	19
14	IILC Algorithm Error	20
15	IILC Region Spectral Comparison	20
16	ILC Weight Chart	21
17	IILC Weight Graph	21
18	IILC 3-y Weight Graph	22
19	Percentage Errors at $\ell=600$	22
20	IILC Unsmoothed Stages	23
21	Basic ILC Maps	23
22	Unsmoothed IILC Maps & Difference	24
23	NILC Input β Maps	25
24	NILC Pixel Maps and Normalisation	26
25	NILC Output Map Comparison	27

List of Tables

1	Input Map Beam-widths	8
2	Percentage Errors at given ℓ	16
3	Required Maps	18
4	Required Notebooks	18
5	Synthetic foreground frequency relations	18
6	Cubature Point and j-Scale Relations	19
7	Basic ILC Weights	28
8	IILC Weights - Unsmoothed 1y	28
9	IILC Weights - Unsmoothed 3y	29
10	Scale-specific NILC normalisation factors	30

1 Introduction

Full, undistorted CMB maps are necessary for statistical observation and analysis with respect to large angular frequencies (Ichiki, 2014). While it is known that the CMB is largely isotropic, with a temperature fluctuation of only $30\mu K$ (Ryden, 2017), the small anisotropies can be difficult to observe as a result of a variety of foreground emissions. Analysis of the CMB as a whole sky map requires a structured cleaning method, without which the CMB can only be observed through aggressive masking of the galactic plane, the source of the most dominant foregrounds.

The method selected for foreground removal is highly dependent on the prior knowledge of the CMB or foreground parameters, where systems like Wiener Inversion (Delabrouille and Cardoso, 2007) and Commander (Eriksen et al., 2006) estimate these. These methods are however highly dependent on the inputs and can introduce biases in their cleaned maps as a result. Instead, it is chosen to use Internal Linear Combination (ILC), a blind component method that assumes as little as possible about the foregrounds before removal.

The foregrounds of the CMB can be considered as three categories where diffuse galactic emission dominate over extra-galactic emission and solar system emission (Delabrouille and Cardoso, 2007). Figure 1 shows the regions of dominance for different diffuse galactic foregrounds. The CMB is most observable in the 44-100GHz range, while it is suppressed heavily in the other bands observed by Planck.

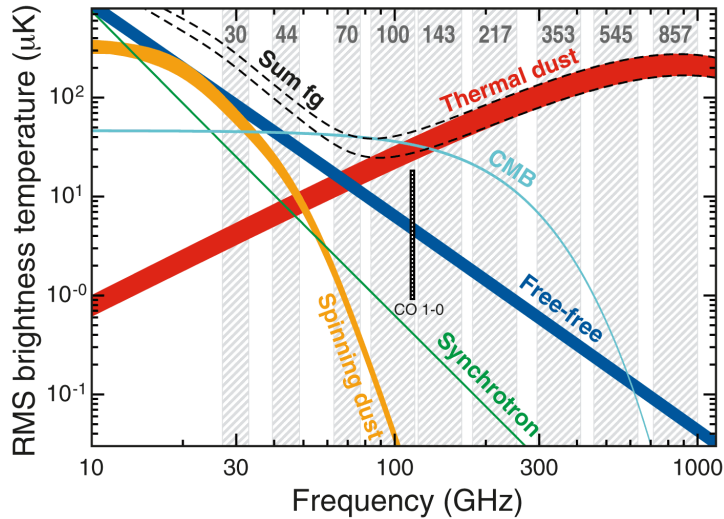


Figure 1: Brightness temperature of foregrounds and the CMB as a function of the frequency, with the grey backgrounds representing the bands covered by the Planck satellite (Planck 2015 X, Adam, Ade, Aghanim, Alves, et al., 2016). The 30, 70, 143 and 353GHz maps are used throughout the different ILC processes in this paper.

It will be necessary to approximate a series of input maps to observe the capability of the ILC models. The important foregrounds to be considered in this approximation are synchrotron, free-free, dust and anomalous (spinning) dust. Each foreground is assumed to have a simple

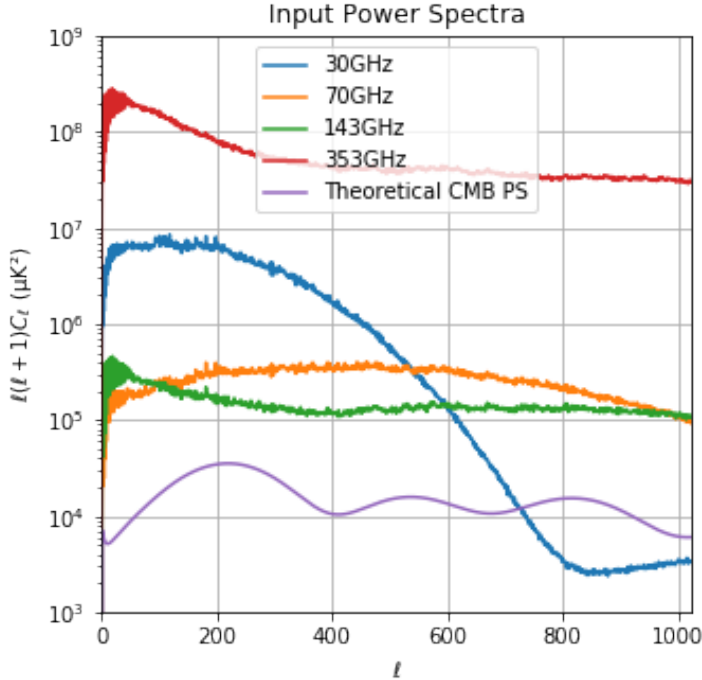


Figure 2: Power spectra of the four Planck maps used in each ILC process, using a logarithmic y axis. These maps show no relation to the theoretical map and as such would be unusable for any analysis of the CMB.

relation to the desired map frequency (Samtleben et al., 2007). This is explored further in section 3 and table 5.

The general goal of the paper is to develop a series of cleaned CMB maps. All the ILC approaches are developed in line with processes pioneered on WMAP inputs (Bennett et al., 2003) (Hinshaw et al., 2007), however the use of Planck maps here makes direct comparison less valuable. As the most extensive method used in this paper loosely follows the NILC method (Basak and Delabrouille, 2011), the quality of cleaning will primarily be compared to the Planck NILC map (Adam, Ade, Aghanim, Arnaud, et al., 2016).

2 Theory

2.1 Internal Linear Combination

The ILC is considered a blind method, with few assumptions made about the foreground. It is necessary to assume the CMB is emitted across all frequency maps, as is expected of a black-body. The process below follows Delabrouille and Cardoso, 2007, where p denotes the space being used, in this case the system is formalized for harmonic space, a choice explained further in section 2.3. In harmonic space, instrumental noise is limited to small angular scales.

Equation 1 expresses the assumption of linear independence between the CMB (s), foregrounds (f_i), and noise (ε_i) across each input map (y_i):

$$y_i(p) = s(p) + f_i(p) + \varepsilon_i(p). \quad (1)$$

To produce an estimate map, \hat{s} , it is necessary to minimize the variance across the inputs through the application of weights specific to each input map,

$$\hat{s}(p) = \sum_i w_i(p) y_i(p). \quad (2)$$

The existence of frequency dependent foregrounds increases variance. Through the requirement that the CMB signal is fully recoverable, the weights can be seen to be applied to the noise and foregrounds directly in equation 3,

$$\hat{s}(p) = s + \sum_i w_i f_i(p) + \sum_i w_i \varepsilon_i(p). \quad (3)$$

To fulfil the requirement of an unmodified CMB signal, the weightings must sum to 1 across all input maps. This allows the explicit generation of individual weights in equation 4,

$$w_i = \frac{\sum_j [C]_{ij}^{-1}}{\sum_i \sum_j [C]_{ij}^{-1}}. \quad (4)$$

The inverse of the covariance of each map, $[C]_{ij}^{-1}$ is calculated simply with NumPy (Harris et al., 2020).

The basic ILC calculates covariance across the whole sky, where the method begins to break down. The linear relation may not hold up well around the galactic plane, while some foregrounds, such as synchrotron emission, vary massively over galactic latitudes making them more difficult to clean. It can be necessary to either mask out sections of the galactic plane before undergoing ILC, or to improve the method itself to account for this.

2.2 Iterative ILC

Through the separation of the input maps into 12 regions, following the process of Bennett et al., 2003, the ILC is able to better clean the input maps. The iterative method consists of masking the input maps to only include a single region, wherein the ILC weights are calculated to best clean this region alone. The selected region on each map is then replaced and another region is selected. After all regions have been cleaned, a single output map is available, however it is necessary to smooth the regions to 1.5° prior to selection to blur the discontinuities that would otherwise develop between each region (Hinshaw et al., 2007).

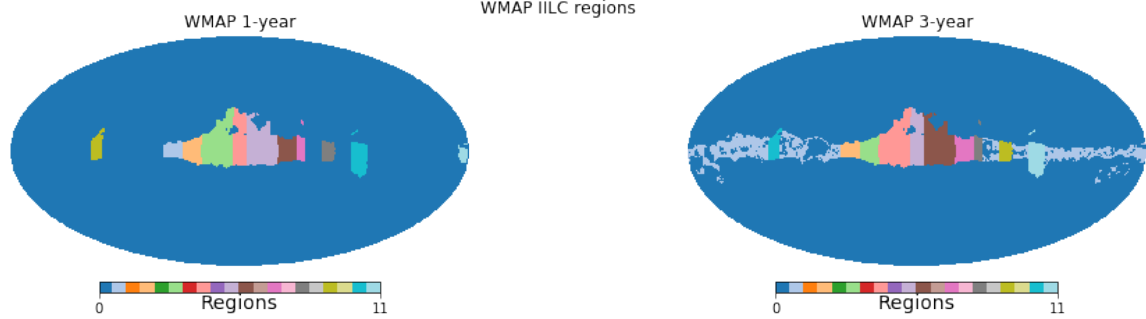


Figure 3: The 12 regions selected by the WMAP 1-year (Bennett et al., 2003) and 3-year (Hinshaw et al., 2007) teams for the iterative method. Both input maps are used, allowing for observation of the quality improvement through minor region corrections.

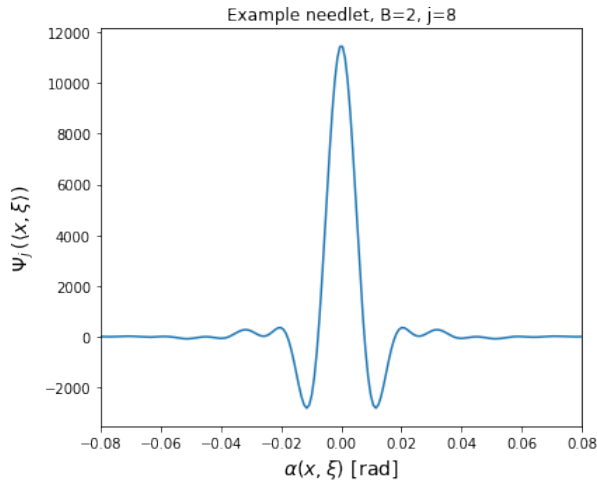


Figure 4: The form of a needlet, Ψ , using the parameters of the NILC method. The needlet itself is not required in the NILC method, only its coefficients. A variety of needlets are used, with j varying between 0 and 11, allowing the system to define coefficients for $\ell = 2048$.

2.3 Needlet ILC

While the above processes are undergone in harmonic space, NILC uses the formation of a separate space entirely, needlet space. This space allows the system the advantages of both pixel and harmonic space. Pixel space analysis does not account for the instrumental noise being limited to small scales, contrary to foregrounds dominating at large scales. Similarly, harmonic analysis cannot account for the inherent variation over latitudes (Basak and Delabrouille, 2011).

Needlet space looks to overcome these disadvantages by filtering the harmonics of the maps into a series of scales, j , in which individual needlets, Ψ , are constrained over angles. An example needlet is shown in figure 4, however, the form of the needlet is not required for the ILC method as the coefficients, β , are used and these can be found without the needlets themselves.

The NILC process is performed on the coefficients of the needlets, β_{jk} , where k refers to a given pixel (Basak and Delabrouille, 2011). As these are pixel dependent, the β maps can be

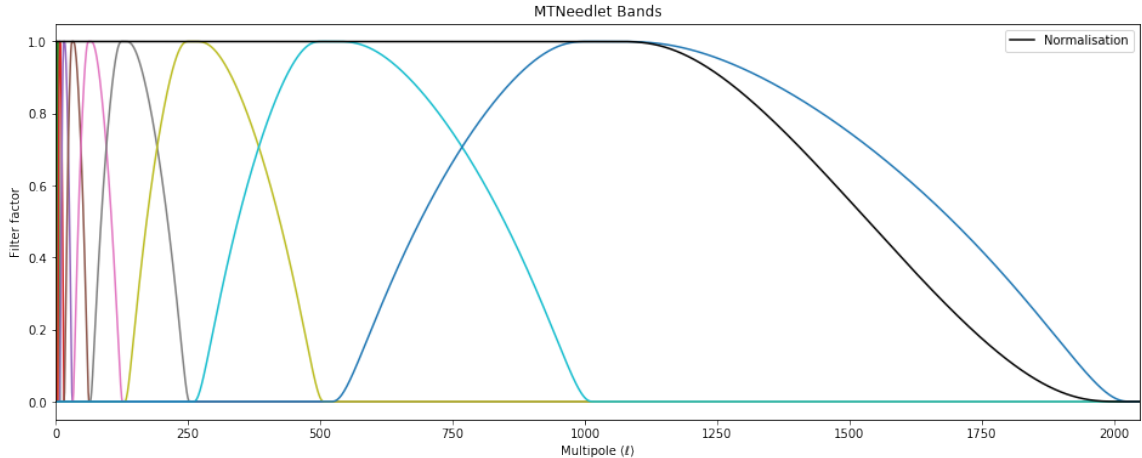


Figure 5: Filters used to separate the input maps in the needlet method. The filters are chosen through MTneedlet (Carrón Duque et al., 2019) and are chosen to normalize to 1. Here, $B = 2$ and j extends to 11.

treated like any other input map to the ILC, with the additional step of recombination of the filtered maps after the ILC process. Here, $a_{\ell m}$ refers to the harmonic coefficients of the map, while $Y_{\ell m}(\xi_{jk})$ defines a series of pixels at given cubature (or quadrature) points on the map in pixel space.

$$\beta_{jk} = \sqrt{\lambda_{jk}} \sum_{\ell=0}^{\ell_{\max}} \sum_{m=-\ell}^{\ell} h_{\ell}^j a_{\ell m} Y_{\ell m}(\xi_{jk}) \quad (5)$$

Similarly, ξ_{jk} and $\sqrt{\lambda_{jk}}$ refer to the cubature points on a sphere and their respective weights. These are explored further in the methodology. h_{ℓ}^j refers to the filter function for a given j (equation 6), calculated externally by the MTneedlet python package (Carrón Duque et al., 2019). These filters are shown in figure 5, the peaks of each filter can be seen to be 2^j . The filters are chosen to allow complete recombination of the original map.

$$h_{\ell}^j = b \left(\frac{\ell}{B^j} \right) \quad \text{where} \quad \sum_j \left(h_{\ell}^j \right)^2 = 1 \quad (6)$$

3 Methodology

Due to the nature of full sky maps, the project must be undertaken computationally. The primary module used for map presentation and harmonic transformations is healpy (Zonca et al., 2019), a HEALIPix¹ wrapper for Python. NumPy (Harris et al., 2020) is also used throughout the code. Tables 3 and 4 provide details on all the maps and notebooks used below.

Before the ILC is performed on any maps, re-scaling of the input maps is required, as the LFI and HFI are given at $N_{side} = 1024$ and 2048 respectively. In the basic and needlet methods,

¹<http://healpix.sourceforge.net>

all maps are scaled to $N_{side} = 1024$, while the WMAP iterative region maps limit the IILC method to $N_{side} = 512$, this is chosen over up-scaling the region maps as the process may blur the edges of regions beyond usability.

It is also necessary to convolve each map to the same band resolution (Basak and Delabrouille, 2011). This process is done simply in healpy by applying a ratio of Gaussian beams, using the smallest beam width of the group (353GHz) over each map's width (table 1), consistent with the more clearly defined convolution method of Rogers et al., 2016.

Input Map	Mean FWHM (arcmin)
LFI 30GHz	32.239
LFI 70GHz	13.252
HFI 143GHz	7.248
HFI 353GHz PSB	4.818

Table 1: Input Map Beam-widths used to convolve maps to the smallest FWHM (Ade et al., 2014) (Aghanim et al., 2014).

3.1 Synthetic Maps and Bias Estimation

To explore the capability of the ILC system in a cleaner environment, synthetic maps must be tested. These maps are developed using the Planck NILC map (Adam, Ade, Aghanim, Arnaud, et al., 2016) as a basis upon which foregrounds are stacked using a series of simple relations derived from Samtleben et al., 2007, expressed in table 5 in the appendix. By using the NILC map as a basis, it is possible to compare the source and output CMB in both power spectra and pixel basis, where regions of bias may become more obvious.

To reduce bias, the four maps used were selected to include very different foregrounds, this will decrease the cross-correlation of unwanted signals. While four maps were used, this was due to computational expense and could be increased to include any number of input maps.

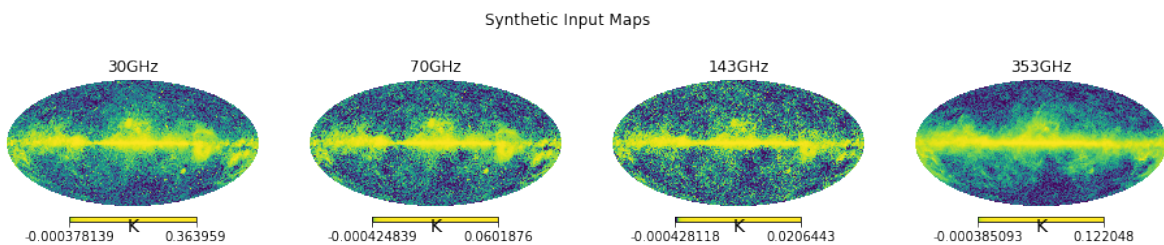


Figure 6: Synthetic foregrounds generated for use in assessment of each ILC method. With the Planck NILC map as a basis, it is possible to compare the clean map directly to its expected source map.

3.2 Basic ILC Method

The basic ILC method requires the four input maps are convolved as above and subsequently run through a series of functions. This process was broken down to allow some analysis of the received weights for each map. The pipeline of functions requires the maps to first be

transformed into alms and then bundled into a list. The functions are flexible to any number of input maps, only requiring the new maps to be added to the list of maps and the relevant beam width added to the FWHM_set list.

Explicitly, the pipeline involves these basic pre-processing steps: rescaling all maps to the same N_{side} , transformation to harmonic space via the defined harmonic function, grouping maps into a list, and convolving to the same beam resolution. Masked analysis requires masking the maps before they are transformed.

Subsequently, the list is fed through cov_inv, taking care to remove $m = 0$ from the alms. This is required by Delabrouille and Cardoso, 2007 and is easily achieved by removing the first value from each array. The map-specific weights are calculated via weight_gen. The weights are checked to sum to 1, there is often an error of approximately 10^{-19} in the imaginary component, but this is a result of floating point errors and is certainly negligible. The alms of each map have their weights applied and are combined and reverted to a single map with output_map.

3.3 Iterative Method

The regions used in IILC must first be extracted from the WMAP maps, where the N_obs column determines the region. These foregrounds are then smoothed with hp.smoothing to 1.5° (Hinshaw et al., 2007), requiring more careful construction of the iterative method. The ILC process is completed using the same functions, with the caveat of the introduction of region_multi_replace, the function used to step through the regions to be processed and replaced. After the completion of the ILC across region 0, region_multi_replace is looped over the remaining 11 regions, allowing a partial map through each iteration (figure 20).

3.4 Needlet Method

An additional process is required in needlet analysis, the input maps must be filtered to a series of maps at given scales. The filters are generated via MTneedlet (Carrón Duque et al., 2019), using a filter width of 2.0. The code is again designed to be flexible, and the filters easily change to cover all scales, including 0, where $1 + \log_2(2048)$ filters are necessary (table 6).

The filters must be applied to the maps in harmonic space and are designed to allow full recombination to the original filtered map, however this process is not direct and some normalization of the resultant map is required. The normaliser function uses np.ptp to rescale the map with respect to the range of temperatures. Each input map required the same rescaling of 3550. This factor will be applied to the NILC output map upon reconstitution.

Equation 5 can be heavily simplified with healpy as the generation of cubature points and

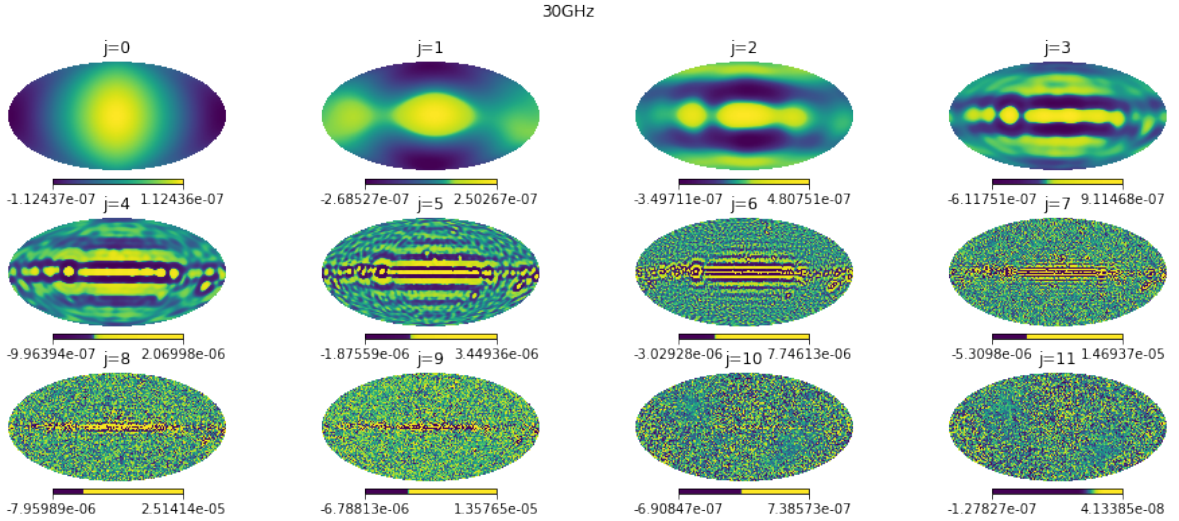


Figure 7: The 30GHz input map has been filtered into the 12 necessary maps to cover all scales to ℓ_{max} . These can be recombined to recover the original map, after applying a normalization factor of approximately 3547.24.

weights with sums over ℓ and m are contained in the healpy function `alm2map` with an N_{side} of the relevant cubature resolution (table 6). The conversion back from β to $a_{\ell m}$ is again, simply `hp.map2alm`, again requiring normalization to combine the filters.

The ILC process is again mimicked, however weightings are formed for each of the 12 β maps, which are then combined and converted back to pixel maps and combined, requiring further normalization (table 10). This breaks from the method proposed by the Planck NILC team (Basak and Delabrouille, 2013), which performed localized ILC, however there are problems with the current implementation (discussed in section 6.2) so that was not attempted.

4 Results

The analysis of a map's cleanliness is best observed in its power spectrum, where signals at larger ℓ can be observed. Each of the output maps is compared to a theoretical CMB (Lewis et al., 2000) map and further analysis is performed with respect to the Planck NILC map (Adam, Ade, Aghanim, Arnaud, et al., 2016). Each output map is provided in the appendix.

Error estimation is discussed in section 6.1.

4.1 ILC Maps

In comparison to the uncleaned foregrounds (figure 2), the basic ILC map massively improves the quality of signal, yet it is not clear enough to be used in any CMB analysis. The large residual foreground remains visible across the galactic plane (figure 21).

The two COMMANDER masks provide substantial improvement. The common mask covers most of the galactic plane in a goal to remove the foregrounds with high confidence, however

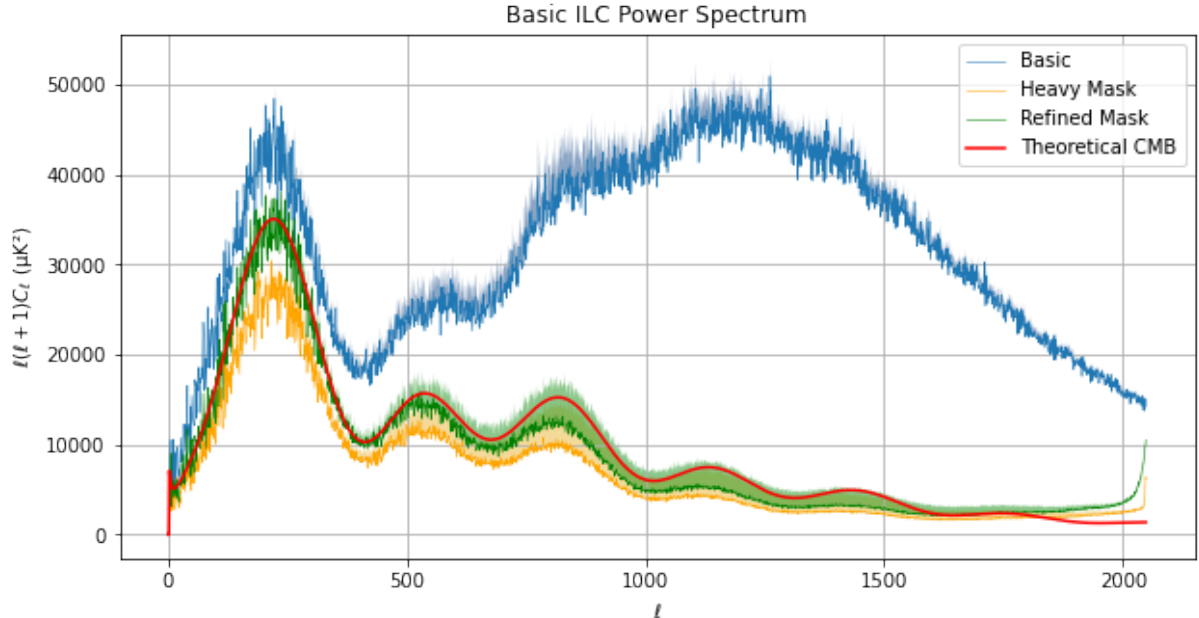


Figure 8: The resulting power spectra from the three ILC cleaned maps, where 'heavy mask' refers to the larger common mask. The masks can be seen to massively improve the spectrum, making it clear that residual foregrounds exist after the initial cleaning process, requiring an improved method. Both masks underestimate the theoretical spectrum as a result of their missing pixels.

it is obvious that this removes too much of the foreground signal to provide a usable power spectrum. This mask covers 22% of the map, limiting usability in CMB analysis over large angles. The smaller infill mask more precisely removes only the regions of the strongest foreground, allowing for a much smaller loss of data, visible in the figure as a closer spectrum out to approximately $\ell = 500$. By offering such a dramatic improvement over the unmasked inputs, it is obvious that substantial foreground remains and an improved method to account for this is necessary.

It can be seen in figure 16 that weights are heavily dominated by the 143GHz map and 30GHz is heavily suppressed, this is consistent with the theory, where the middle frequency maps have the least foreground.

Accounting for the systematic underestimation seen through synthesis, the refined mask slightly overestimates the theoretical CMB until high ℓ , where noise begins to dominate.

4.2 IILC Maps

It is natural to compare the output IILC maps to the best result of the prior method, the refined mask. It is not particularly valuable to observe power spectrum differences as a result of the 1-year and 3-year regions, these largely overlap (figure 15). The two output maps appear near-identical at a glance, but the 3-year can be seen as slightly cleaner in figure 22. Figures 17 and 18 visualize the distribution of weights across all 12 regions. These primarily follow the expected bias towards around the 70GHz and 143GHz maps, however region 1 in the 3-year

map swaps dominance, with the 70GHz map accounting for the most weight, highlighted in blue in table 9. This is to be expected, as region 1 largely mimics the foreground observed in the 70GHz input map.

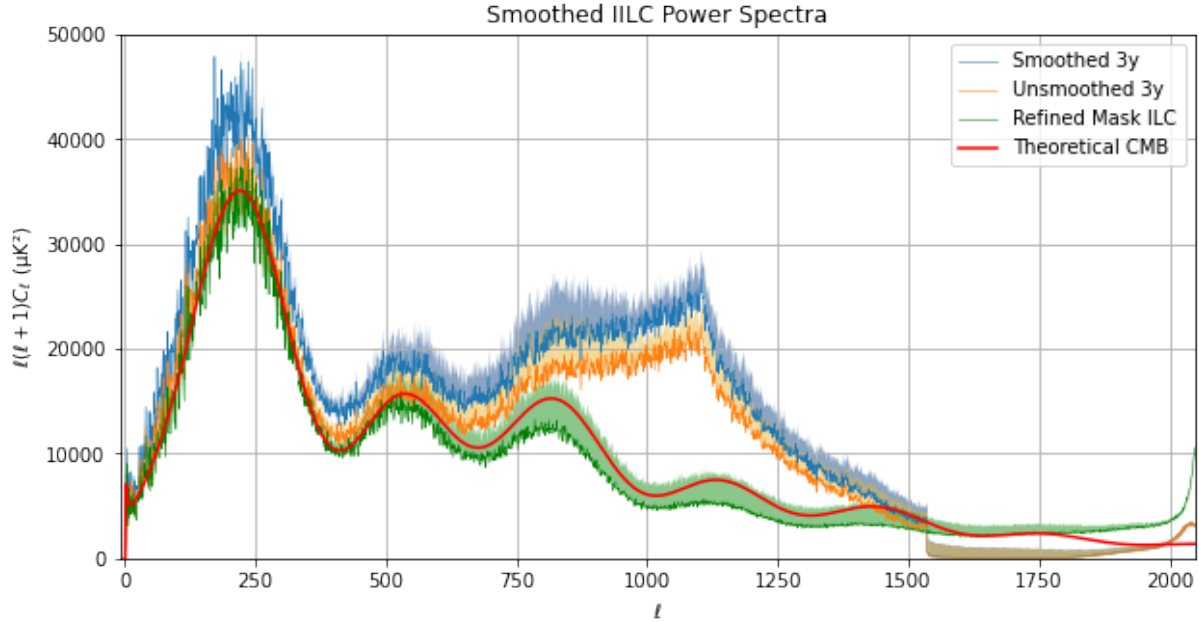


Figure 9: IILC cleaned maps compared to the best ILC map. The IILC maps present strong correlation to the theoretical out to $\ell \approx 300$, with foreground noise taking over until ≈ 1100 . From there, discontinuities are expected to be the cause of the unusual shape out to $\ell = 1535$. The sudden cut-off at 1535 has no known cause.

It was expected that the act of smoothing the regions to 1.5° would remove the unusual shape visible from $\ell > 1100$, however this was not the case when applied, it is likely the method in which this smoothing was done was mistaken, as this in fact made the output map worse. The believed source of this error is around the selection of regions via Boolean and then applying their local smoothing. The output map does not have any apparent noise in these cross-over areas, which would otherwise present a more obvious problem with the method.

4.3 NILC Map

While all attempts were made to develop a working form of the NILC, the system was not able to recover a viable map.

Figure 23 shows the four input maps split into their constituent scale maps, each sub-map having a power between 10^{-8} and 10^{-5} . The output NILC scale maps unusually do not follow this, however, instead ranging from 10^{-7} and 10^{-6} , inhibiting recombination. It was chosen to normalize these pixel maps against Planck NILC filtered pixel maps at the same scales, bringing the output values in line (figure 24, table 10).

The inclusion of complex values in the normalization suggests that the pixel maps have not fully undergone transformation, as these should not be present in this space.

Figure 25 shows a loss of detail in the map, observable as a suppression in the power spectrum above very low ℓ , making the map unsuitable for CMB analysis.

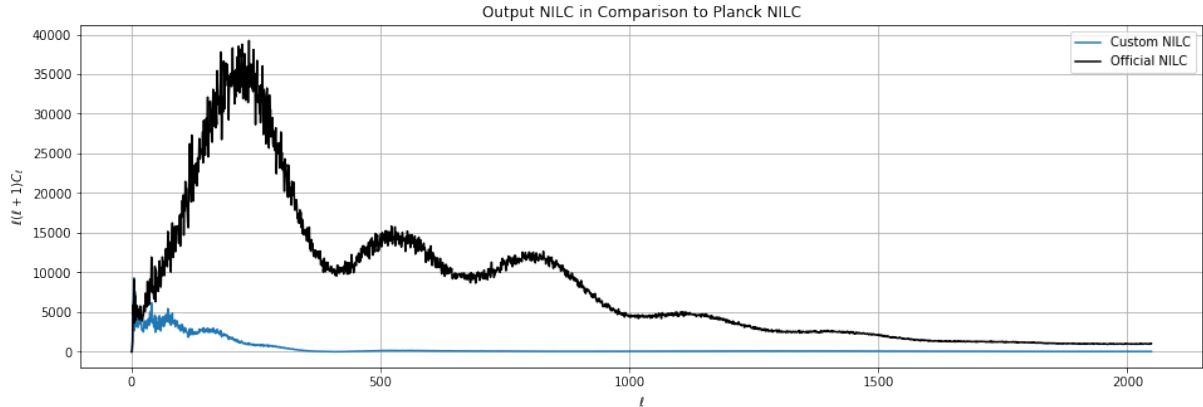


Figure 10: NILC map power spectrum. The map suffers from heavily suppressed values beyond very low ℓ , making it unusable.

Further observations of the faults are explored in section 6.2.

5 Conclusion

With the goal of producing a foreground-cleaned map with a power spectrum that strongly followed the theoretical CMB (Lewis et al., 2000) through internal linear combination, a series of near-usable maps were created. A simple masked version offers competition with Planck’s NILC map (Adam, Ade, Aghanim, Arnaud, et al., 2016) out to $\ell \approx 1500$, with an error of 1.1% less than NILC, while forfeiting pixels to the mask.

Ultimately, the ILC is most valuable for statistical analysis of the CMB when masks are not used, so attempts were made to explore the iterative and needlet ILC methods to improve on the strong basic ILC method. However, these systems were not able to provide power spectra comparable to that of Planck’s NILC map, the ultimate goal of the project. The unsmoothed IILC is only slightly less capable than the Planck NILC out to $\ell \approx 900$ before extraneous behaviour overcomes the spectrum. The iterative method failed to improve when regions were applied smoothly, likely the result of inappropriate masking. Further investigation is likely to improve the performance.

A working needlet basis was formed and given more time, the NILC method may have become usable, as the limiting factor was recovery through β conversion. Further efforts into this system, or perhaps infilling for masked regions combined with the IILC would dramatically improve the quality of map available.

References

- Adam, R., Ade, P. A. R., Aghanim, N., Alves, M. I. R., Arnaud, M., Ashdown, M., Aumont, J., Baccigalupi, C., Banday, A. J., & et al. (2016). Planck2015 results. *Astronomy and Astrophysics*, 594, [Graph]. <https://doi.org/10.1051/0004-6361/201525967>
- Adam, R., Ade, P. A. R., Aghanim, N., Arnaud, M., Ashdown, M., Aumont, J., Baccigalupi, C., Banday, A. J., Barreiro, R. B., & et al. (2016). Planck2015 results. *Astronomy and Astrophysics*, 594, A9. <https://doi.org/10.1051/0004-6361/201525936>
- Ade, P. A. R., Aghanim, N., Alves, M. I. R., Arnaud, M., Ashdown, M., Aumont, J., Baccigalupi, C., Banday, A. J., Barreiro, R. B., & et al. (2016). Planck2015 results. *Astronomy & Astrophysics*, 594, A25. <https://doi.org/10.1051/0004-6361/201526803>
- Ade, P. A. R., Aghanim, N., Armitage-Caplan, C., Arnaud, M., Ashdown, M., Atrio-Barandela, F., Aumont, J., Baccigalupi, C., Banday, A. J., & et al. (2014). Planck2013 results. vii. hfi time response and beams. *Astronomy & Astrophysics*, 571, A7. <https://doi.org/10.1051/0004-6361/201321535>
- Aghanim, N., Armitage-Caplan, C., Arnaud, M., Ashdown, M., Atrio-Barandela, F., Aumont, J., Baccigalupi, C., Banday, A. J., Barreiro, R. B., & et al. (2014). Planck2013 results. iv. low frequency instrument beams and window functions. *Astronomy & Astrophysics*, 571, A4. <https://doi.org/10.1051/0004-6361/201321544>
- Basak, S., & Delabrouille, J. (2013). A needlet ilc analysis of wmap 9-year polarization data: Cmb polarization power spectra. *Monthly Notices of the Royal Astronomical Society*, 435(1), 18–29. <https://doi.org/10.1093/mnras/stt1158>
- Basak, S., & Delabrouille, J. (2011). A needlet internal linear combination analysis of wmap 7-year data: Estimation of cmb temperature map and power spectrum. *Monthly Notices of the Royal Astronomical Society*, 419(2), 1163–1175. <https://doi.org/10.1111/j.1365-2966.2011.19770.x>
- Bennett, C. L., Hill, R. S., Hinshaw, G., Nolta, M. R., Odegard, N., Page, L., Spergel, D. N., Weiland, J. L., Wright, E. L., Halpern, M., & et al. (2003). First-year wilkinson microwave anisotropy probe (wmap) observations: Foreground emission. *The Astrophysical Journal Supplement Series*, 148(1), 97–117. <https://doi.org/10.1086/377252>
- Carrón Duque, J., Buzzelli, A., Fantaye, Y., Marinucci, D., Schwartzman, A., & Vittorio, N. (2019). Point source detection and false discovery rate control on cmb maps. *Astronomy and Computing*, 28, 100310. <https://doi.org/https://doi.org/10.1016/j.ascom.2019.100310>
- Delabrouille, J., & Cardoso, J. (2007). *Diffuse source separation in cmb observations*. arXiv: astro-ph/0702198
- Eriksen, H. K., Dickinson, C., Lawrence, C. R., Baccigalupi, C., Banday, A. J., Gorski, K. M., Hansen, F. K., Lilje, P. B., Pierpaoli, E., Seiffert, M. D., & et al. (2006). Cosmic mi-

- crowave background component separation by parameter estimation. *The Astrophysical Journal*, 641(2), 665–682. <https://doi.org/10.1086/500499>
- Harris, C. R., Millman, K. J., van der Walt, S. J., Gommers, R., Virtanen, P., Cournapeau, D., Wieser, E., Taylor, J., Berg, S., Smith, N. J., Kern, R., Picus, M., Hoyer, S., van Kerkwijk, M. H., Brett, M., Haldane, A., del Río, J. F., Wiebe, M., Peterson, P., ... Oliphant, T. E. (2020). Array programming with NumPy. *Nature*, 585(7825), 357–362. <https://doi.org/10.1038/s41586-020-2649-2>
- Hinshaw, G., Nolta, M. R., Bennett, C. L., Bean, R., Dore, O., Greason, M. R., Halpern, M., Hill, R. S., Jarosik, N., Kogut, A., & et al. (2007). Three-year wilkinson microwave anisotropy probe (wmap) observations: Temperature analysis. *The Astrophysical Journal Supplement Series*, 170(2), 288–334 [Graph]. <https://doi.org/10.1086/513698>
- Ichiki, K. (2014). CMB foreground: A concise review [06B109]. *Progress of Theoretical and Experimental Physics*, 2014(6). <https://doi.org/10.1093/ptep/ptu065>
- Lewis, A., Challinor, A., & Lasenby, A. (2000). Efficient computation of CMB anisotropies in closed FRW models. *American Journal of Physics*, 538, 473–476. <https://doi.org/10.1086/309179>
- Rogers, K. K., Peiris, H. V., Leistedt, B., McEwen, J. D., & Pontzen, A. (2016). SILC: a new Planck internal linear combination CMB temperature map using directional wavelets. *Monthly Notices of the Royal Astronomical Society*, 460(3), 3014–3028. <https://doi.org/10.1093/mnras/stw1121>
- Ryden, B. (2017). *Introduction to cosmology* (2nd ed.). Cambridge University Press.
- Samtleben, D., Staggs, S., & Winstein, B. (2007). The cosmic microwave background for pedestrians: A review for particle and nuclear physicists. *Annual Review of Nuclear and Particle Science*, 57(1), 245–283. <https://doi.org/10.1146/annurev.nucl.54.070103.181232>
- Zonca, A., Singer, L., Lenz, D., Reinecke, M., Rosset, C., Hivon, E., & Gorski, K. (2019). Healpy: Equal area pixelization and spherical harmonics transforms for data on the sphere in python. *Journal of Open Source Software*, 4(35), 1298. <https://doi.org/10.21105/joss.01298>

6 Appendix

6.1 Errors & Synthetic Analysis of the Methods

Through analysing the result of synthetic inputs through each method, it is possible to observe the base systematic error as a result of weakness in the algorithm. The output maps are simply compared to the Planck NILC basis on which the synthetic maps were formed, any deviation can be assumed to be a result of poor cleaning. Furthermore, the application of minor Gaussian noise to the input maps can explore the result of irremovable small-scale

noise on the power spectra. Figures showing the difference between the NILC and different algorithms are presented in section 6.3. The underestimation shown in figure 13 could be a result of a flawed smoothing method applied to the formed synthetic maps, however if the loss of power is consistent, it may account for underestimation in the true output maps, which are properly smoothed.

Percentage errors were calculated by standard means (equation 7) and plotted with a Gaussian smoothing factor. When citing a calculated average error over a region, care was taken to ensure these are taken from unsmoothed values. An example diagram is expressed in figure 19. Errors have been calculated across a series of ℓ , as it may be prudent to only use a given map out to a limited ℓ for improved accuracy.

$$\varepsilon = \left| \frac{\hat{s} - s_{theory}}{s_{theory}} \right| \times 100 \quad (7)$$

Method	Average ε over ℓ (%)					
	300	600	900	1200	1500	2048
Masked ILC	7.55	6.19	8.72	12.3	15.6	28.2
Unsmoothed IILC 3-y	9.66	7.96	12.2	47.6	49.2	56.6
Smoothed IILC 3-y	25.7	24.8	30.4	72.6	73.1	73.5
Planck NILC	7.39	5.65	8.01	12.1	16.7	18.1

Table 2: Average percentage error of each ILC method out to given ℓ . Highlighted values indicate errors that exceed the maximum average error seen by the Planck NILC (18.1%), which can be considered too great to be usable.

6.2 NILC failings

As a sanity check, it is necessary to observe the needlet recovery on a system that has not undergone ILC. This process was performed, presenting a fault in the system more obviously. The system is incapable of fully recovering a signal, as presented in figure 11, where signal is lost between filters 8 and 9 (figure 12). Further analysis at different ℓ_{max} was able to move the missing region, but not remove it. Without fixing this fault, the NILC process will not provide a valid output map.

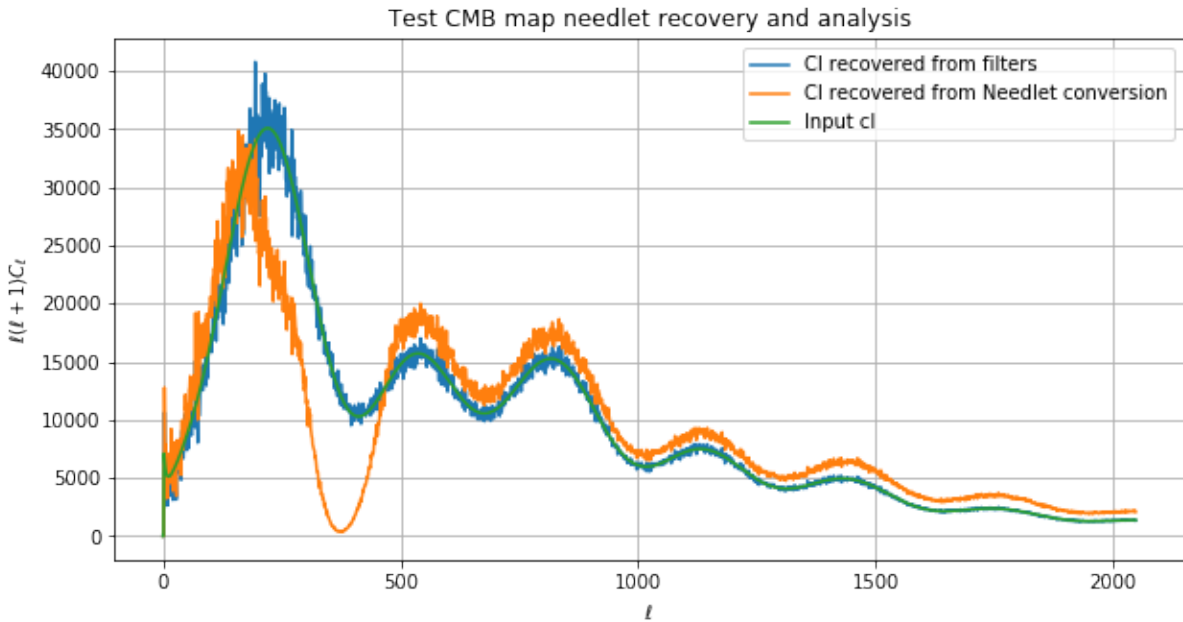


Figure 11: Recovery from needlet conversion on a single input map. The recovered map fails to represent the input, having lost power in the 256-512 regions. The cause of this is unknown.

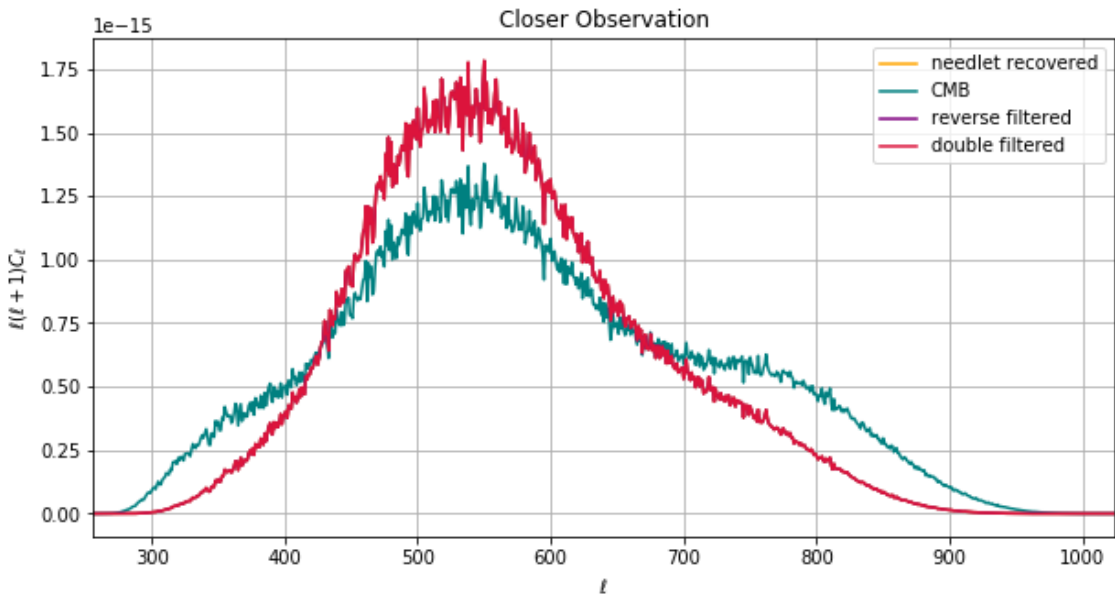


Figure 12: Closer observation of the failing region. The yellow and purple lines are identical to the red. Any application of the filter process produces a different shape than the initial CMB spectrum. The double filtered process particularly should recover exactly the CMB form, but does not.

6.3 Excess Tables and Diagrams

Imported Map	Usage	File Name	Source
LFI 30GHz	All ILC	LFI_SkyMap_070fieldIQU_1024_R3.00_full.fits	PLA ¹
LFI 70GHz	All ILC	LFI_SkyMap_030fieldIQU_1024_R3.00_full.fits	PLA
HFI 143GHz	All ILC	HFI_SkyMap_143fieldIQU_2048_R3.00_full.fits	PLA
HFI 353GHz PSB	All ILC	HFI_SkyMap_353psbfieldIQU_2048_R3.00_full.fits	PLA
Heavy	ILC Mask	COM_Mask_CMBcommonMaskInt_2048_R3.00.fits	PLA
Refined	ILC Mask	COM_Mask_CMBlnpaintingMaskInt_2048_R3.00.fits	PLA
NILC	Synthesis	COM_CMB_IQUnilc_2048_R3.00_full.fits	PLA
Synch FG	Synthesis	COM_CompMap_Synchrotroncommander_0256_R2.00.fits	PLA
F-F FG	Synthesis	COM_CompMap_freefreecommander_0256_R2.00.fits	PLA
Dust FG	Synthesis	COM_CompMap_dustcommander_0256_R2.00.fits	PLA
A-Dust FG	Synthesis	COM_CompMap_AMEcommander_0256_R2.00.fits	PLA
1-year Regions	IILC	wmap_ilc_rgn_defn_yr1_v1.fits	LAMBDA ²
3-year Regions	IILC	wmap_ilc_rgn_defn_3yr_v2.fits	LAMBDA

Table 3: All Maps mentioned in the paper and used in the supplied code, listing their download sources and particular uses. 1: <https://pla.esac.esa.int/#maps> 2: https://lambda.gsfc.nasa.gov/product/map/dr2/ilc_map_get.cfm

Method	File Name
ILC	ILC_method_convolved.ipynb
IILC Smoothed	Iterative_ILC_smoothed.ipynb
IILC Unsmoothed	Iterative_ILC_single_resolution.ipynb
NILC	NILC_refined.ipynb
Synthesis	guided_synthetic_maps.ipynb

Table 4: Attached notebooks with relevant code for the project. Diagrams were largely created externally.

Foreground	Reference Frequency (GHz)	Simple Temperature relation
Synchrotron	0.408	$T_{synch}^{synth} \approx T_{synch}^{Com} \cdot \left(\frac{\nu}{\nu_{synch}} \right)^{-3.1}$
Galactic Dust	545	$T_{dust}^{synth} \approx T_{dust}^{Com} \cdot \left(\frac{\nu}{\nu_{dust}} \right)^3$
Free-Free	4	$T_{ff}^{synth} \approx T_{ff}^{Com} \cdot \left(\frac{\nu}{\nu_{ff}} \right)^{-2.14}$
Anomalous Dust	22	$T_{adust}^{synth} \approx T_{adust}^{Com} \cdot \left(\frac{\nu}{\nu_{adust}} \right)^{-2.5}$

Table 5: Simple relations between synthetic temperature maps and the COMMANDER foreground maps used in approximating synthetic maps for ILC analysis (Adam, Ade, Aghanim, Alves, et al., 2016) (Ade et al., 2016). The COMMANDER foregrounds must first be converted from μ K to K.

j	ℓ_{peak}	$N_{pix} = \text{cubature points, } \xi_{jk}$
0	1	12
1	2	48
2	4	192
3	8	768
4	16	3072
5	32	12288
6	64	49152
7	128	196608
8	256	786432
9	512	3145728
10	1024	12582912
11	2048	50331648

Table 6: Cubature points and filter peaks for given scales, j , used in the needlet analysis.

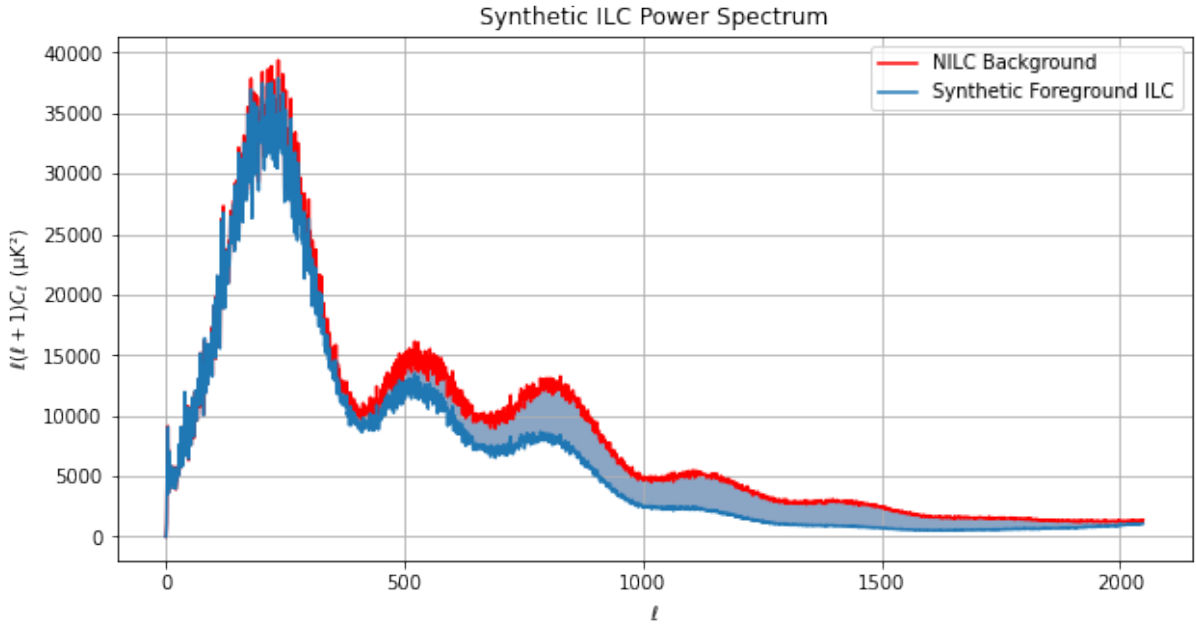


Figure 13: The difference between the cleaned ILC map and underlying CMB map (red) can be used to estimate systematic error in the method. The difference between the two is presented as a band here and is used in the subsequent bands of the basic ILC power spectra.

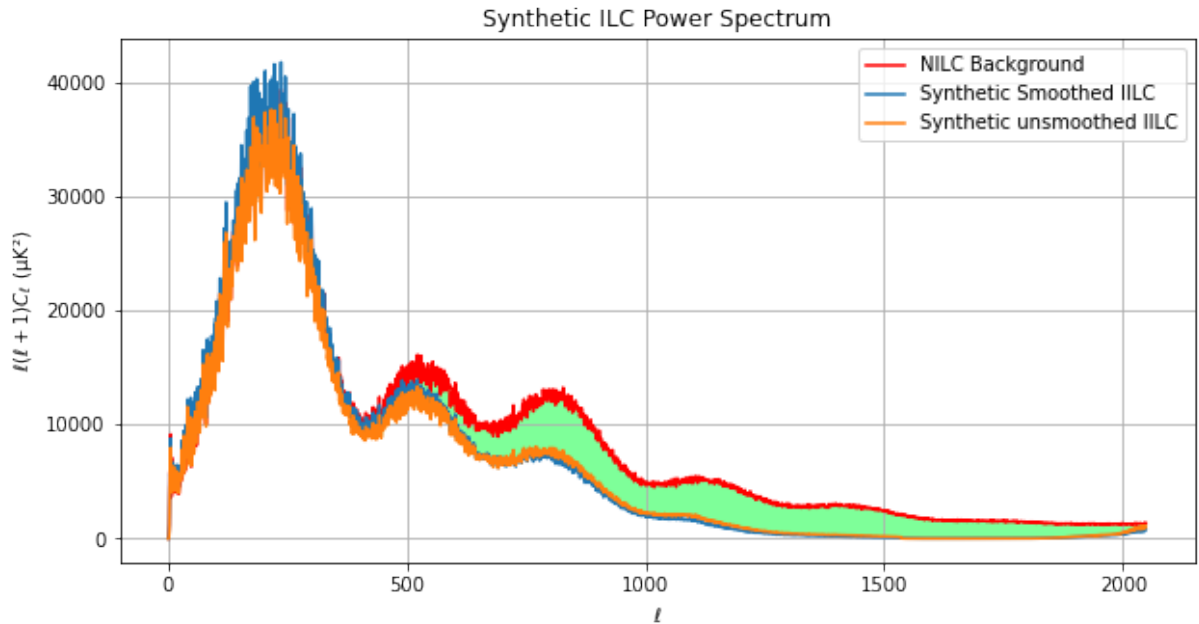


Figure 14: Systematic error of the IILC smoothed and unsmoothed processes, completed in the same manner as figure 13.

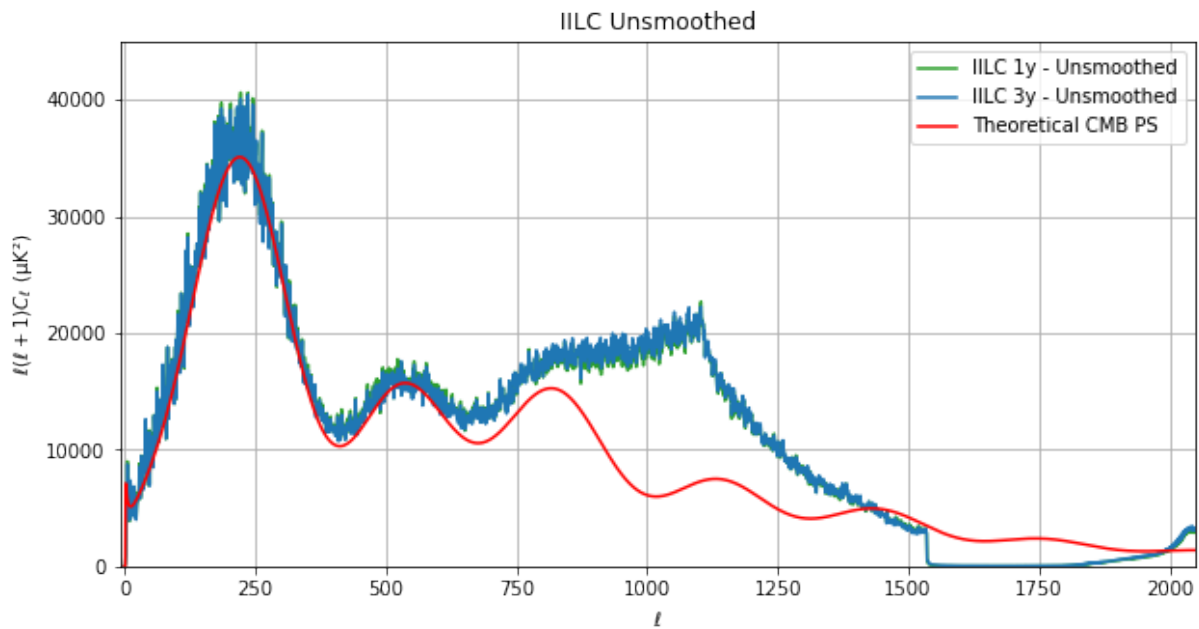


Figure 15: The difference observed between the 1 and 3-year IILC regions is almost negligible, the two regions largely overlap. There is an observable difference in the visible maps (figure 22), but not in this graph.

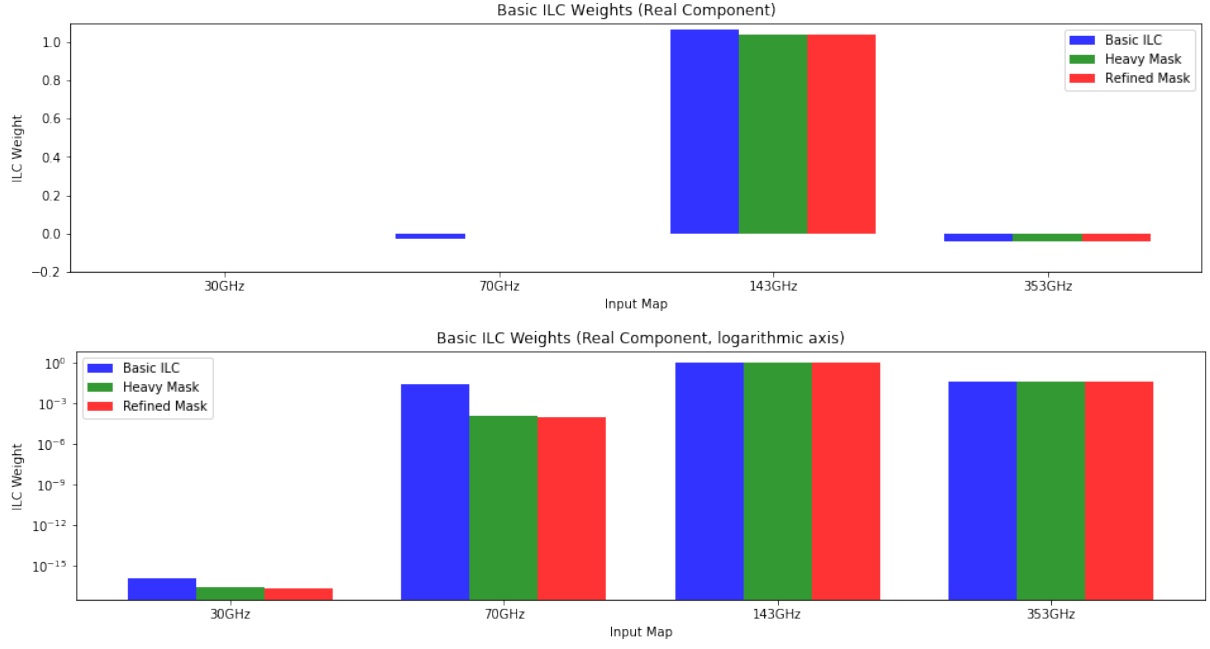


Figure 16: Visualization of the weights associated with each cleaned map. Both charts represent the same data, however the lower map uses a logarithmic y-axis to better present the sheer dominance of the 143GHz map, which influences all weights, while 30GHz is suppressed greatly. This is consistent with the theory.

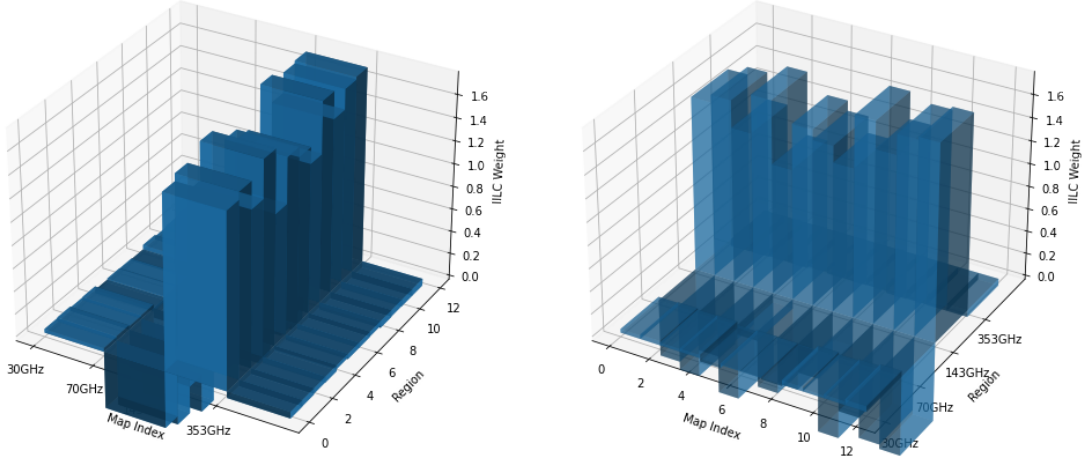


Figure 17: Visualizations of the real weights associated with each map across the twelve 1-year regions in the unsmoothed IILC. The base axes are swapped to view the obscured data. The 143GHz map again dominates, however the 70GHz takes a greater weighting than the base ILC and there are no j-scale regions that deviate massively from the trend. The data can be viewed directly in table 8.

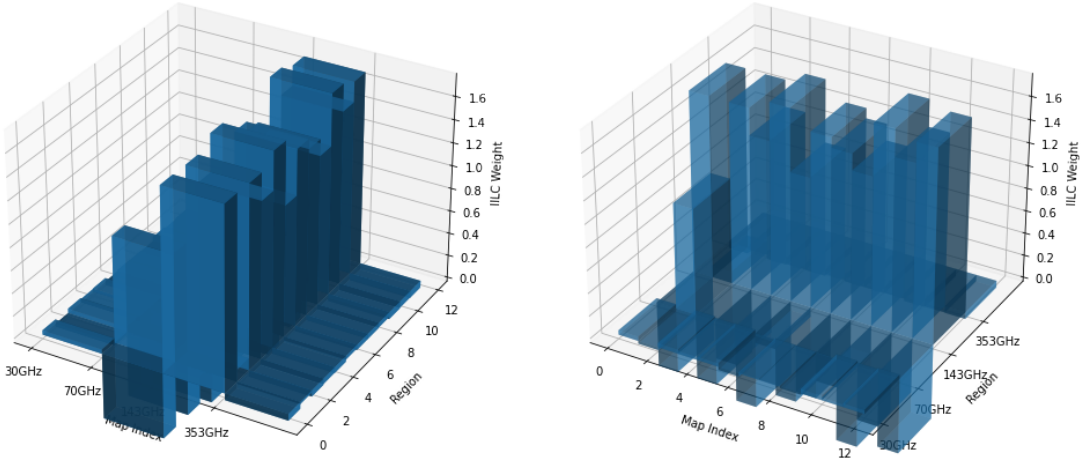


Figure 18: Visualizations of the real weights associated with each map across the twelve 3-year regions in the unsmoothed IILC. The base axes are swapped to view the obscured data. Region 1 bucks the trend, wherein the 70GHz map is momentarily dominant. This is highlighted in blue in table 9.

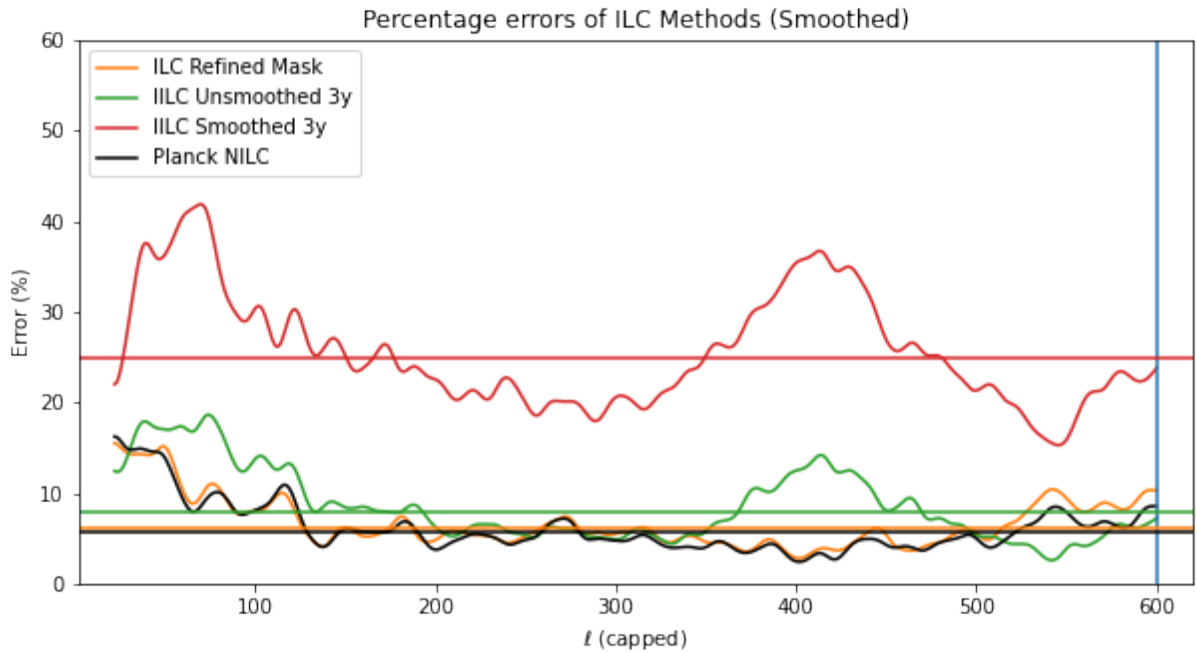


Figure 19: Percentage Errors (smoothed with a Gaussian beam upon plotting) and the average percentage error of each system at $\ell=600$.

6.4 Additional Maps

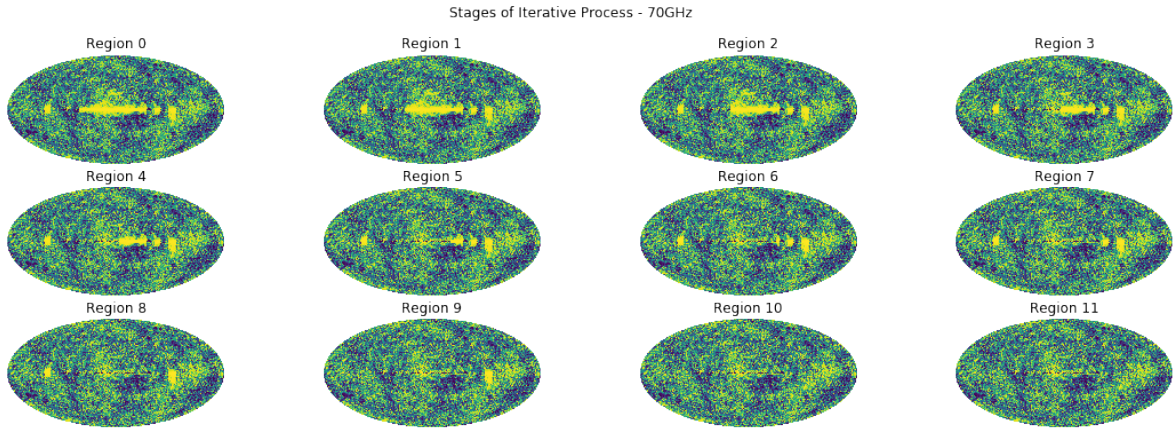


Figure 20: Stages of the iterative process without smoothing the 1-year WMAP regions. The process cleans a region and pastes it into the map in succession. This map shows the 70GHz uncleaned map as the starting point, but the map outputted by region 11 is identical to all other cleaned frequency maps.

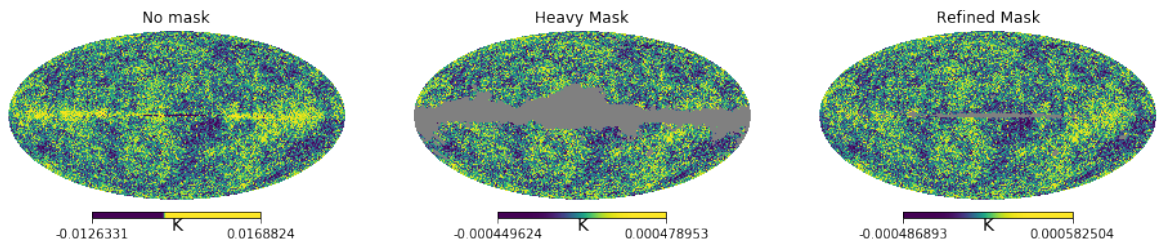


Figure 21: The three Basic ILC output maps, with the centre and right maps using COMMANDER's common and infill masks respectively. The unmasked map includes a substantial residual foreground that renders analysis of the power spectrum useless.

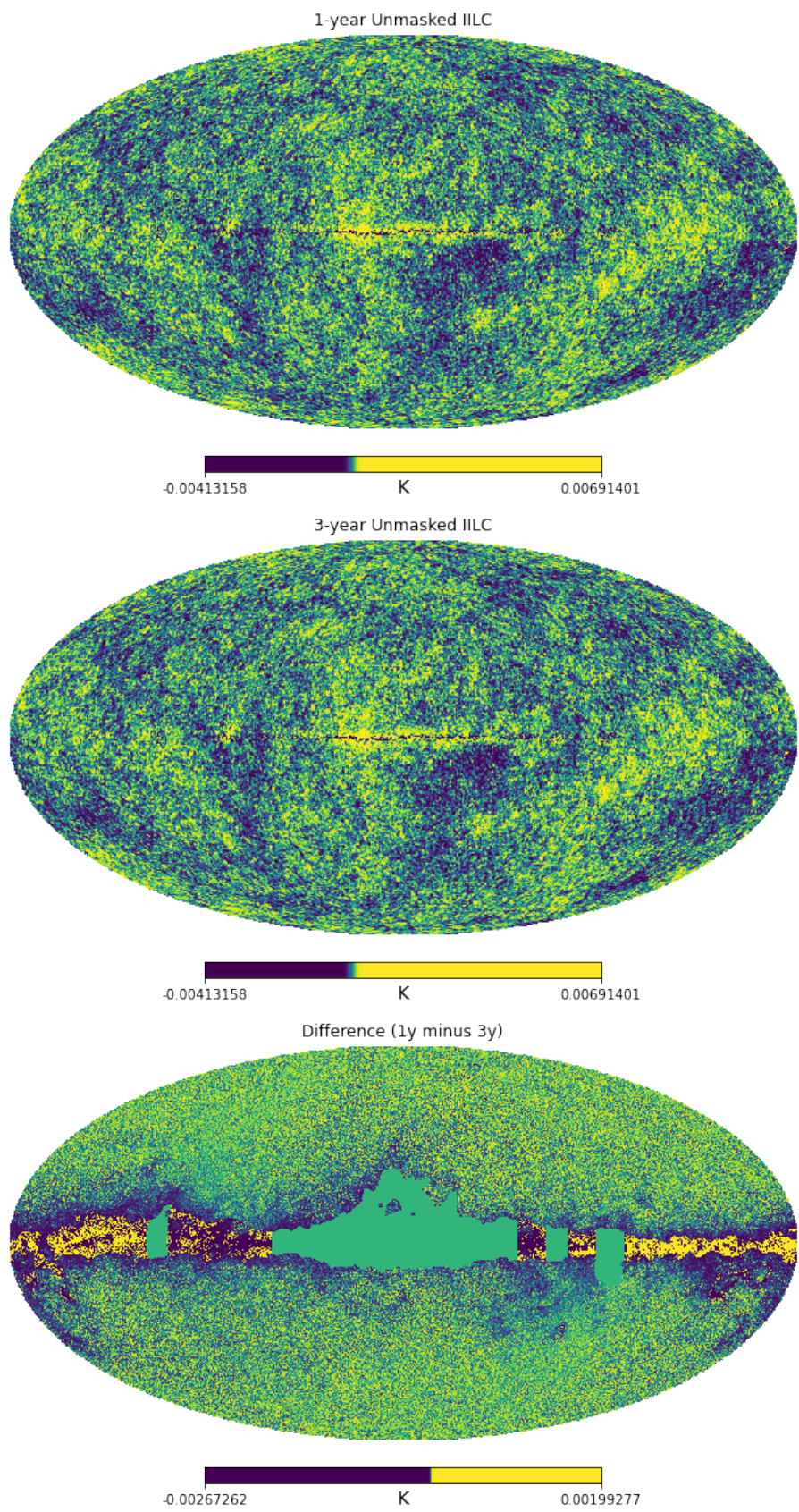


Figure 22: Unsmoothed 1 and 3-year IILC maps respectively. The difference is the residual of 1-y when 3-y is subtracted, to better show the changes. The variation only exists in the modified regions.

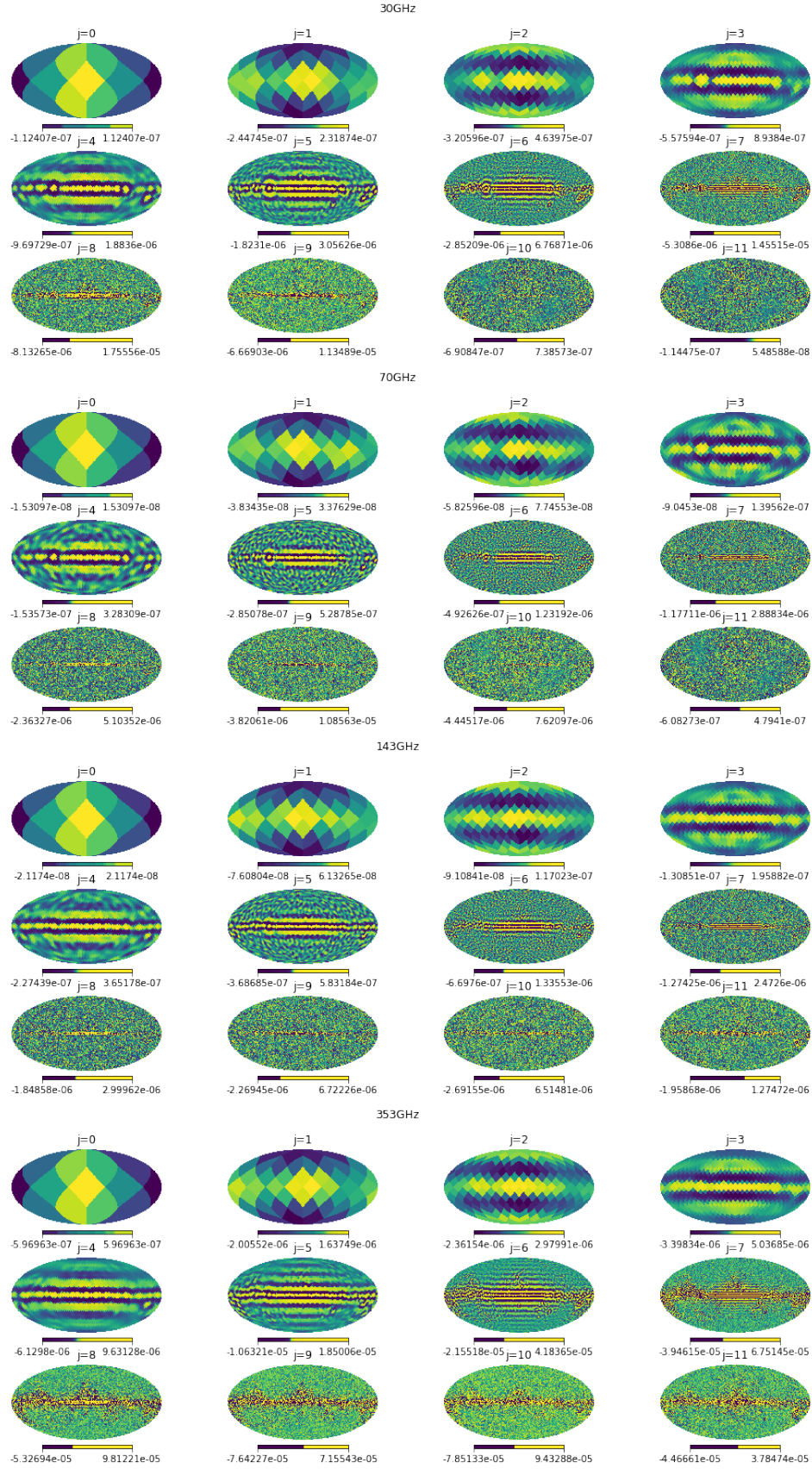


Figure 23: Needlet Coefficient (β) maps for each scale (j) of each input map. All maps range from $e-5$ to $e-7$ and show strong scale-dependent forms. This behaviour is lost in the output NILC β maps.

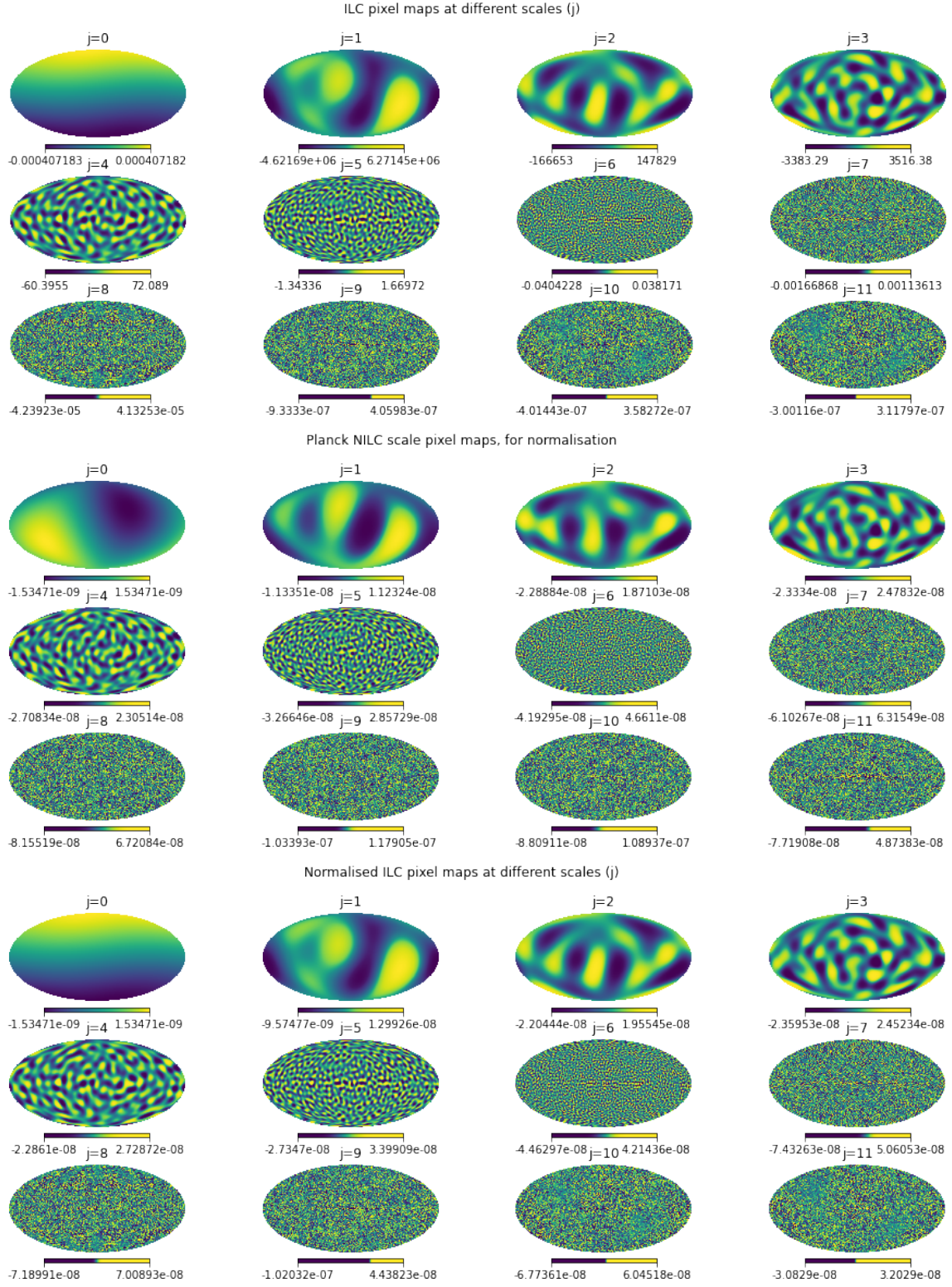


Figure 24: Output NILC pixel maps, which exhibits great variation in power across different scales. By normalising with respect to the filtered Planck NILC (middle), a more usable output can be generated. Normalization factors included in section 6.5.

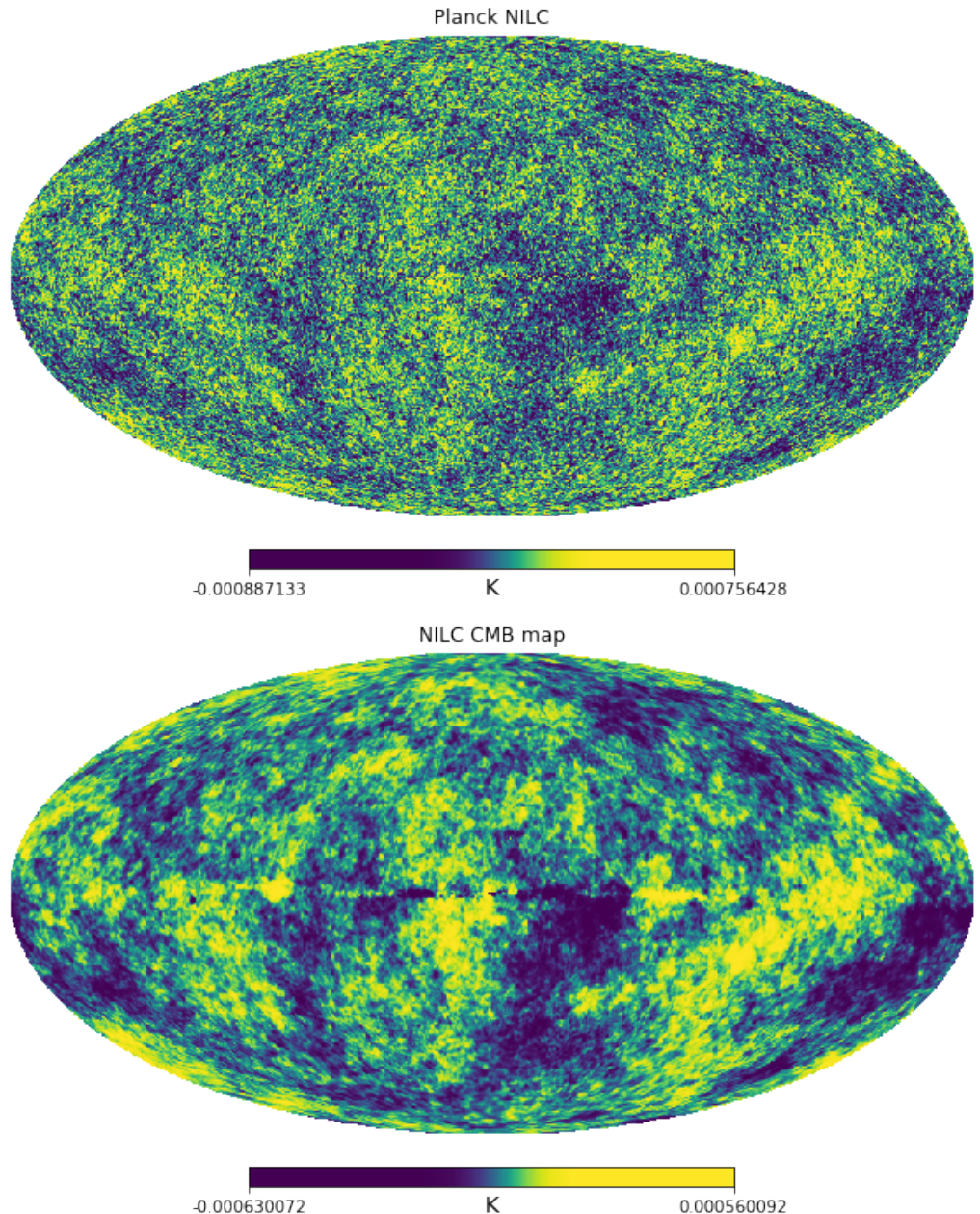


Figure 25: It is clear that the output NILC map is not competitive with the Planck map, all details above even the lowest ℓ is suppressed.

6.5 Data

Input Map	Unmasked weight	Common mask weight	Infill mask weight
30GHz	5.94e-17	-1.95e-17	-1.86e-17
	1.03e-16j	1.85e-17j	9.44e-18j
70GHz	-2.78e-02	1.21e-04	1.05e-04
	-2.17e-04j	2.62e-05j	2.34e-05j
143GHz	1.07	1.04	1.04
	2.75e-04j	7.31e-04j	-1.44e-04j
353GHz	-4.10e-02	-4.28e-02	-4.20e-02
	-5.78e-05j	-7.57e-04j	1.21e-04j

Table 7: Weights generated for the three ILC maps.

Region	Map	IILC Weight	Map	IILC Weight
0	30GHz	0.0322+0.00101j	70GHz	-0.508-0.00102j
1		0.0389 +0.000877j		-0.582-0.0135j
2		0.0274-0.00411j		-0.342+0.02380219j
3		0.0319+0.00386j		-0.674-0.00507467j
4		-0.0286-0.000282j		-0.0851+0.01164696j
5		0.0101+0.00117j		-0.504-0.00488578j
6		0.00655+0.00294j		-0.412-0.01660963j
7		-0.0116 +0.00252j		-0.255-0.0090263j
8		0.0404-0.00403j		-0.736 +0.04622564j
9		0.0249+0.000893j		-0.489-0.00043561j
10		0.0348-0.00704j		-0.672+0.02913617j
11		0.0509+0.000631j		-0.712+0.00019574j
0	143GHz	1.53-0.000184j	353GHz	-0.0572+0.000190j
1		1.60+0.0128j		-0.0548-0.000181j
2		1.36-0.0206j		-0.0479+0.000865j
3		1.69+0.00137j		-0.0510-0.000150j
4		1.16-0.0112j		-0.0321-0.000191j
5		1.54+0.00406j		-0.0457-0.000345j
6		1.45+0.0145j		-0.0459-0.000817j
7		1.31+0.00709j		-0.0422-0.000575j
8		1.76-0.0436j		-0.0624+0.00137j
9		1.52-0.00101j		-0.0578+0.000548j
10		1.70-0.0229j		-0.0608+0.000783j
11		1.73-0.000688j		-0.0608 -0.000139j

Table 8: Weights generated for the unsmoothed 1-year IILC map.

Region	Map	IILC Weight	Map	IILC Weight
0	30GHz	0.0382+0.000355j	70GHz	-0.585+0.00153j
1		-0.0244+0.00140j		0.937 -0.0590j
2		0.0389+0.000877j		-0.582-0.0135j
3		0.0274-0.00411j		-0.342+0.0238j
4		0.0319+0.00386j		-0.674-0.00507j
5		-0.0286-0.000282j		-0.0851+0.0116j
6		0.0101+0.00117j		-0.504-0.00489j
7		0.00655+0.00294j		-0.412-0.0166j
8		-0.0116+0.00251j		-0.255-0.00903j
9		0.0404-0.00403j		-0.736 +0.0462j
10		0.0249+0.000894j		-0.488-0.000436j
11		0.0348-0.00704j		-0.672+0.0291j
0	143GHz	1.605-0.00202j	353GHz	-0.0587+0.000146j
1		0.105+0.0590j		-0.0177-0.00145j
2		1.60+0.0128j		-0.0548-0.000181j
3		1.36-0.0206j		-0.0479+0.000865j
4		1.69+0.00137j		-0.0510-0.000150j
5		1.15-0.0112j		-0.0321-0.000191j
6		1.54+0.00406j		-0.0457-0.000345j
7		1.45+0.0145j		-0.0459-0.000817j
8		1.31+0.00709j		-0.0422-0.000575j
9		1.76-0.0436j		-0.0624+0.00137j
10		1.52-0.00101j		-0.0578+0.000548j
11		1.70-0.0229j		-0.0608+0.000783j

Table 9: Weights generated for the unsmoothed 3-year IILC map. The blue values represent results that break heavily from the general trend across all regions.

j pixel map	Normalization factor
0	0.00341+0.000693j
1	0.00612+0.000168j
2	0.00990+0j
3	0.0125+0j
4	0.0164+0j
5	0.0303+0j
6	0.0790+0j
7	0.239+0j
8	0.905+0j
9	4.22-1.09j
10	11.2+4.59j
11	17.2+4.32j

Table 10: Scale-specific NILC filtered pixel map normalization factors calculated in reference to the Planck NILC map under the same filters. The inclusion of complex values in pixel space exhibits a fault in the code.